Journal of Materials Chemistry A

ROYAL SOCIETY OF CHEMISTRY

PAPER

View Article Online
View Journal | View Issue

Cite this: *J. Mater. Chem. A*, 2024, **12**, 8405

Continuous flash sublimation of inorganic halide perovskites: overcoming rate and continuity limitations of vapor deposition†

Tobias Abzieher, ‡*[a] Christopher P. Muzzillo, ‡[a] Mirzo Mirzokarimov, [a] Gabriella Lahti, [a] Wylie F. Kau, [b] Daniel M. Kroupa, [b] Spencer G. Cira,[c] Hugh W. Hillhouse, [c] Ahmad R. Kirmani, [ae] Jackson Schall, [d] Dana Kern, [a] Joseph M. Luther [a] and David T. Moore *[a]

Despite the outstanding progress in performance of halide perovskite solar cell absorbers fabricated *via* vapor-based approaches, increasing deposition rates as well as enabling continuous deposition has been woefully neglected. In fact, recent reports show deposition times for the fabrication of high performing absorbers typically in the range of hours, being orders of magnitude away from industrially reasonable process times. In this work, continuous flash sublimation (CFS) of halide perovskite absorbers is introduced as a concept to overcome the fundamental rate and continuity limitations of current approaches, while at the same time maintaining the performance of previously reported vapor deposition approaches. Using CFS, we reduce the time required to deposit a fully absorbing layer to less than 5 minutes, demonstrating the applicability of vapor deposited halide perovskites for commercialization. Additionally, the approach enables continuous deposition, thus circumventing another major bottleneck of established vapor deposition approaches.

Received 27th September 2023
Accepted 4th February 2024

DOI: 10.1039/d3ta05881f

rsc.li/materials-a

Introduction

Today, research on halide perovskite materials for opto-electronic applications is dominated by solution-based deposition techniques given their fast progress in a laboratory environment as well as their prospects for future low-cost, high-throughput fabrication.[1,2] However, the transfer of these techniques from laboratory to an industrial environment is challenging and even experienced leaders in the opto-electronic industry are struggling to achieve sufficient production yield and reproducibility when solution-based techniques are implemented into an industrial production chain.[3] It is therefore not surprising that in industry, and in particular in photovoltaic manufacturing, vapor-based deposition techniques still dominate. For example, First Solar, Inc., the industry leader in both cumulative deployed thin-film photovoltaics and thin-film photovoltaics manufacturing capacity, produces their cadmium telluride solar cells by vapor processing.[4–6] Furthermore, organic photovoltaics, which can be fabricated by either solution or vapor methods are commercialized by the Heliatek GmbH using vapor processing.[7] Similar to these technologies, vapor-based processing is expected to play a crucial role in the commercialization of perovskite-based photovoltaics.[8] Not only can they enable a high-quality process with high production yield and reproducibility but also eliminate hazardous solvents and simplify upscaling to larger device areas.[9] In addition, the ability to uniformly coat on rough surfaces is benefited by vapor processing, which is of particular importance when it comes to the deployment of perovskite-based materials in tandem applications.[10–12] While only a small fraction of research in the field is focused on vapor processing of halide perovskite materials, its progress is in no way inferior to solution-based approaches – particularly when it comes to the most studied hybrid organic–inorganic halide perovskite materials.[13–15] Solar cells employing vapor processed organic–inorganic halide perovskite absorbers have demonstrated power conversion efficiencies (PCEs) of 24.4%,[16] being on par with solution-based approaches.[17]

Despite the benefits of vapor-based deposition techniques, two critical issues of vapor processing of halide perovskites remain: (1) their low deposition rates and (2) their lack of continuous deposition. In fact, industrially viable deposition

[a]*National Renewable Energy Laboratory (NREL), Center for Chemistry & Nanoscience Research, Golden, CO 80401, USA. E-mail: david.moore@nrel.gov; tobias.abzieher@gmail.com*

[b]*BlueDot Photonics, Inc., Seattle, WA 98105, USA*

[c]*University of Washington, Department of Chemical Engineering, Seattle, WA 98195, USA*

[d]*Colorado School of Mines, Golden, CO 80401, USA*

[e]*School of Chemistry and Materials Science, Rochester Institute of Technology, Rochester, NY 14623, USA*

† Electronic supplementary information (ESI) available. See DOI: https://doi.org/10.1039/d3ta05881f

‡ T. A and C. P. M contributed equally to this work.

strategies for halide perovskite materials that combine high deposition rates and continuous deposition do not currently exist. These limitations have their origin in the fundamental challenge of depositing multiple materials with significantly different vapor pressures (*i.e.*, $p_{\text{cesium halides}} \ll p_{\text{lead halides}} \ll p_{\text{organic halides}}$), which has predominantly led to the development of deposition approaches defined by the vaporization/sublimation characteristics of the most volatile compounds (*e.g.*, co-evaporation approaches). Although co-deposition has led to high performing devices, the approach has only demonstrated deposition rates between 1 nm min^{-1} and 10 nm min^{-1} resulting in absorber processing times of at least one hour (see Fig. 1, Tables S1, and S2 in the ESI†). Slight progress has been realized by alternative approaches including sequential and chemical vapor deposition (CVD) approaches, however, these demonstrations have come at the expense of performance.[18–22] Currently, the fastest processes are based on single-source flash sublimation in which the deposition process is designed to sublime all compounds simultaneously at a temperature above the sublimation temperature of the least volatile compound.[23] In most of these flash sublimation approaches, a metal foil is coated with a thin film of the target material using solution-based processes and the resulting foil used as the source material for the vapor deposition.[24–27] This two-step process of solution casting followed by vapor deposition is obviously not practical for high-throughput commercial processing, has not demonstrated high performing devices, does not leverage the environmental advantages of vapor processing by removing solvents from the process, and increases the overall processing complexity; as such, these techniques have not been included in Fig. 1 but are tabulated and marked in Tables S1 and S2 in the ESI.† To overcome these limitations, single-source evaporation of pre-synthesized powder has been introduced, however, only in non-continuous batch approaches and with only limited performance compared to state-of-the-art solar cells.[28–34] Surprisingly, the overall trend in low deposition rates even holds for fully inorganic perovskite materials, which one might assume are capable of higher deposition rates. Similar to hybrid perovskite materials, continuous approaches that are able to yield high-quality absorber materials at significantly higher deposition rates do not exist and the highest PCEs for vapor processed inorganic perovskite solar cell absorbers are achieved *via* low-throughput approaches (*i.e.*, layer-by-layer deposition).[35] High-throughput processes (*e.g.*, single source evaporation) of inorganic halide perovskites have been reported to be particularly challenging given the various crystallographic phases in these materials, limiting their PCEs to only 9.0% when integrated into solar cells.[33,36]

In response to these challenges, continuous flash sublimation (CFS), is employed in this work as a continuous, high-throughput vapor deposition technique capable of overcoming the challenges of material systems composed of constituents with largely different vapor pressures. To avoid the decomposition of organic components, while maintaining a large volatility difference in the individual components, we focus here on the all inorganic $CsPbX_3$ materials. We demonstrate the ability of CFS to produce compositions across the entire iodine–bromine space that maintain the composition of

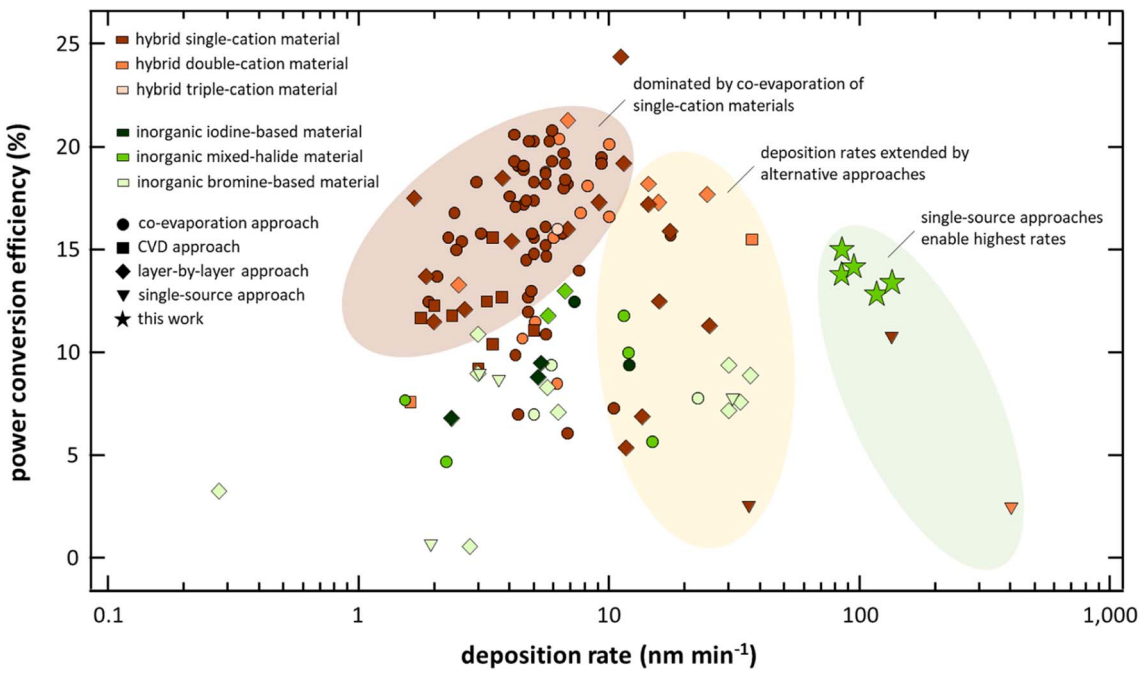

Fig. 1 Summary of power conversion efficiencies of vapor processed hybrid (brown) and inorganic (green) halide perovskite solar cells together with their respective deposition rates. High-efficiency vapor processed solar cells are dominated by co-evaporation approaches of hybrid perovskite materials with deposition rates typically below 10 nm min^{-1}. Detailed information about the individual data points can be found in the ESI.†

the source materials, have a structural evolution equivalent to their co- or solution-deposited analogs, and demonstrate superior compositional and optical homogeneity. Finally, the inclusion of CFS derived films in working solar cells results in device performance that is on par with solution deposited films and superior to any previously reported vapor deposited all-inorganic perovskite devices.

Results and discussion

Continuous flash sublimation – process controllability through simplicity

CFS was first employed as early as 1948 for the deposition of Au/Cd alloys across the entire compositional range in spite of the wide volatility difference between Au and Cd. It is adaptable to continuous operation, and its deposition rates are only limited by the boat size and powder feed rate.[23] In this work a version of CFS is implemented as the challenges for vapor deposited, halide perovskites are similar to those systems for which CFS has been previously employed. Fig. 2 illustrates the three simple steps of the CFS approach developed for the fabrication of inorganic halide thin films in this work. Source material is a mechano-chemically synthesized powder that is prepared by mixing individual precursor materials (*i.e.*, cesium and lead salts) to a stoichiometric powder, followed by a ball milling step for 20 min in inert atmosphere, which ensures a uniform mixing of the individual powder constituents as well as their chemical reaction to perovskite (see discussion below). Next, the powder is filled into a powder reservoir that is connected to a vibratory feeder inside the prototype CFS deposition system. When the vibratory feeder is connected to an AC signal in the frequency range of 40 Hz to 60 Hz the powder is quickly delivered to a boat held at constant temperature. Adjustment of the frequency allows for fine tuning of the powder supply rate (typically in the range of 100 mg min^{-1}) and therefore deposition rate during the process. After transferring the powder along the vibratory feeder, the powder falls into a preheated tantalum evaporation boat kept at a temperature significantly above the highest sublimation temperature of the individual inorganic salts (typical contact temperatures at the boat surface are in the range of 700 °C). Inside the evaporation boat, the powder constituents instantaneously sublime, leave the evaporation source through perforated holes on the opposite side of the evaporation boat, and finally condense on a substrate situated above the evaporation boat that is neither actively cooled nor actively heated in the employed prototype CFS system.

Flash sublimation ensures that films have the same composition as the source material by completely and instantaneously subliming one grain of source material before the next grain arrives,[37] which simplifies process control and monitoring compared to classical co-evaporation approaches substantially. This is of particular importance for source materials whose constituents have highly diverse vapor volatilities like in the case of the cesium and lead halide system investigated in this work, making this material system a particularly suitable testbed for the approach. Most importantly, the process enables processing times of only a few minutes (<5 minutes), surpassing any previously reported fully vapor-based absorber deposition approach, while maintaining the performance compared to significantly slower processes – particularly for inorganic halide perovskite materials (see Fig. 1). Previous work demonstrated batch flash sublimation by adding powder to a boat, pumping down the chamber, and quickly ramping up the boat temperature.[28–34] Here, a critical step toward

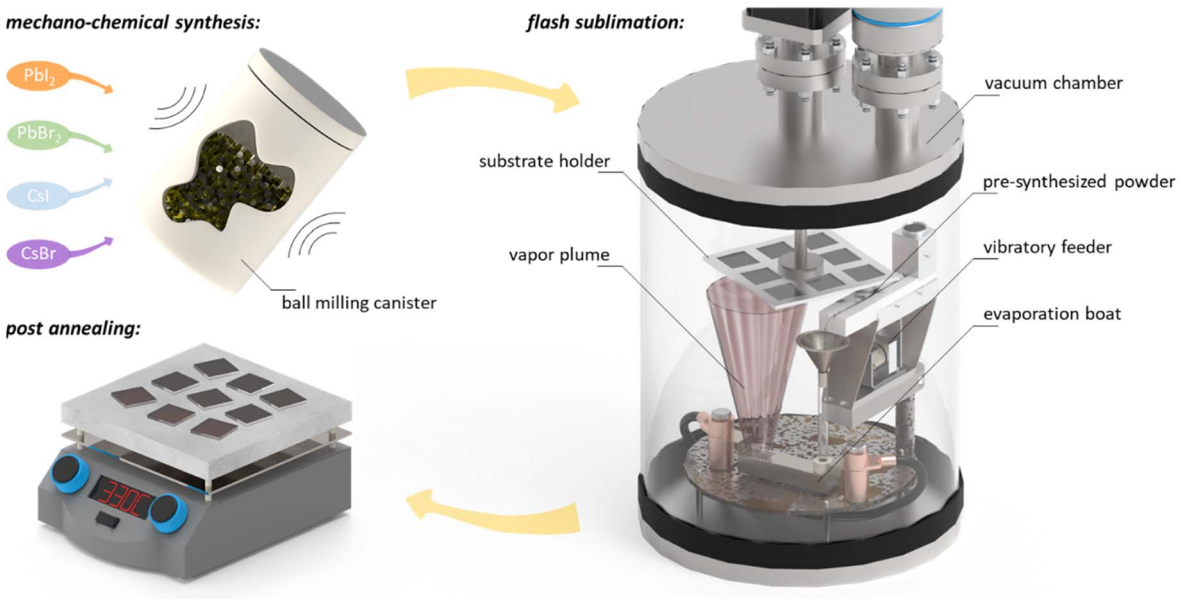

Fig. 2 Schematic illustration of the continuous flash sublimation (CFS) approach consisting of a mechano-chemical synthesis of the source powder (here $CsPb(I_xBr_{1-x})_3$), the high-throughput deposition process in a home-made evaporation system, and a short post-annealing treatment to improve thin-film quality.

continuous processing is demonstrated by enabling a continuous powder supply in which the powder is not exposed to any heat before it reaches the sublimation source. Finally, to improve thin-film quality and to ensure stabilization of the correct photoactive perovskite phase, a short post-annealing step at temperatures between 330 °C and 380 °C for 0.5 min to 1 min in inert atmosphere is performed. Additional details about the process can be found in the experimental section. It needs to be highlighted that the number of process parameters in the CFS approach is reduced to powder composition, powder feed rate, boat temperature, and post-annealing conditions; this reduction of process parameters simplifies process controls and monitoring significantly compared to established vapor processing techniques.

High-quality thin-film formation *via* continuous flash sublimation

The versatility of the developed CFS approach with respect to thin-film composition is shown next based on the fabrication of a variety of high-quality $CsPb(I_xBr_{1-x})_3$ thin films over the full iodine–bromine range. Fabrication of high-quality, high-uniformity inorganic perovskite thin films is known to be challenging – particularly for solution-based approaches – given the strong influence of process parameters on film formation in the complex inorganic system. This has not only led to a variety of rather complex deposition techniques (*e.g.*, antisolvent quenching and gradual annealing procedures) that require adaptation for every specific absorber composition,[38–49] but also results in severe issues when it comes to the upscaling of the deposition process for this material class (see Fig. S1 in the ESI†). In contrast, the CFS approach enables a unique and, so far, unmatched universality with respect to the fabrication of high-quality inorganic thin films with varying iodine–bromine composition. Fig. 3a illustrates the successful realization of high-quality thin films ranging from pure $CsPbI_3$ to pure $CsPbBr_3$ prepared by varying the iodine-to-bromine ratio of the source powder from $x = 0.00$ to $x = 1.00$ (additional photographs from different angles can be found in Fig. S2 in the ESI†). Other than the composition of the source powder (and a slightly higher post-annealing temperature for films with $x > 0.67$), process parameters have not been altered to realize these different compositions, being a significant improvement compared to previously reported more complex approaches.[38–49]

Most importantly, in detailed inductively coupled plasma mass spectrometry (ICP-MS) analyses (see Fig. S3 in the ESI†) it is shown that the composition of the thin films is identical to the (stoichiometric) composition of the source powder indicating a direct translation of the composition from powder to thin film. This highlights the simplicity of fabricating thin films with arbitrary composition by CFS and is also a proof of its flash sublimation nature. In addition, because of the highly uniform deposition process that results in a homogenous nucleation, thin-film formation, and crystal phase properties, upscaling to larger areas is easily achieved without any further adaption of the process (see Fig. S1 in the ESI†). The visual impression ranging from dark black, fully absorbing thin films for higher iodine contents ($x > 0.50$) to reddish and yellowish transparent films for higher bromine contents ($x < 0.50$) follows the expected trend when varying the bandgap of the thin films. Bandgap energies (E_g) extracted from corresponding Tauc plots lie within the range of $E_g = 1.76$ eV for pure iodine thin films and $E_g = 2.36$ eV for pure bromine films (see Fig. 3b),[50,51] while intermediate compositions follow a linear trend as typically observed for a substitutional solid solution (see Fig. S4 in the ESI†). While most of these

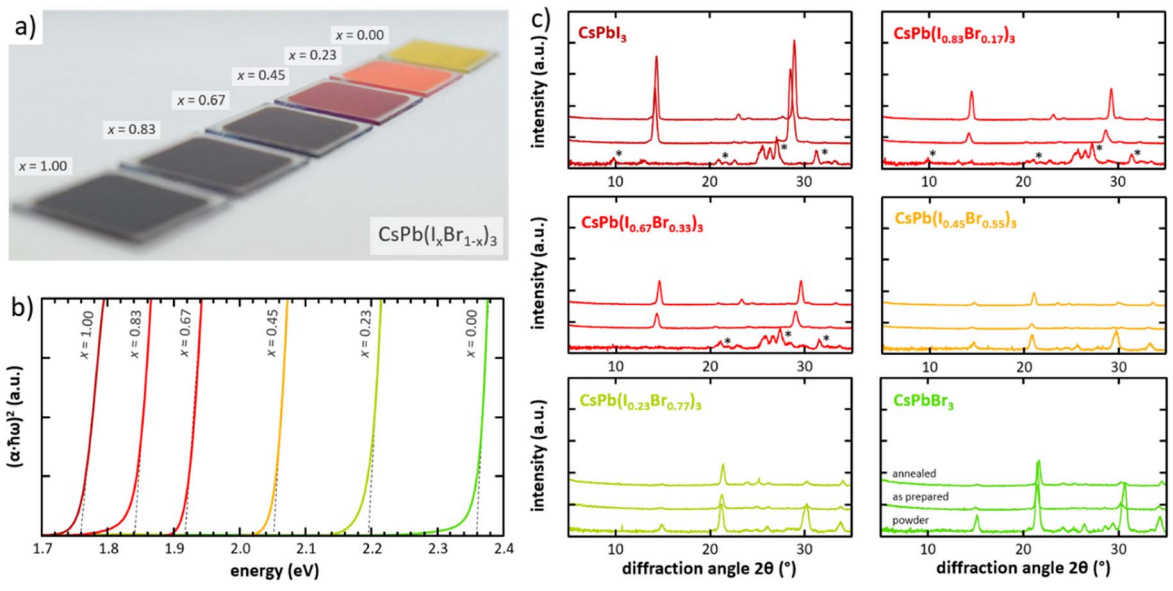

Fig. 3 High-quality fabrication of $CsPb(I_xBr_{1-x})_3$ thin films by CFS with varying iodine-to-bromine ratios. (a) Photograph of thin films with different bandgap energies. (b) Tauc plots with extrapolated bandgap energies for thin films with different iodine-to-bromine ratios. (c) Crystallographic properties of mechano-chemically synthesized source powders (bottom line), as-prepared thin films (middle line), and post-annealed thin films (top line). Peaks that are linked to the occurrence of the photoinactive δ-phase are marked with asterisks.

higher-bandgap materials are rather inappropriate for the use in single-junction solar cells, they are of particular interest for multi-junction solar cell concepts as well as for light-emitting devices. Next to outstanding uniformity and simple tunability of the bandgap energy, excellent crystallographic properties of the resulting thin films are a particular characteristic of the herein developed CFS approach. Fabrication of high-quality inorganic perovskites is significantly complicated given their complex crystallographic phase setting. Next to various photoactive perovskite phases (*i.e.*, cubic (α), tetragonal (β), and orthorhombic (γ) phases), whose formation and presence at room temperature as well as influence on the opto-electronic properties of the thin films are still not fully understood, the photoinactive hexagonal (δ) phase is another competing phase that is stable at room temperature but detrimental to the performance of opto-electronic devices.[52–55] Various procedures to stabilize one of the photoactive phases at room temperature exist particularly for solution-based approaches, however, they are typically unique to the exact thin-film composition as well as the deposition approach. Conversely, versatile strategies that can be adapted for a wide range or even the full range of inorganic thin-film compositions are rare.[38–49] In the following it is shown that the CFS approach is intrinsically able to produce photoactive perovskite thin films over the complete iodine-to-bromine ratio (see Fig. 3c). All source powders employed in this work are prepared in a low-temperature mechano-chemical process (*i.e.*, ball milling). Stabilization of the photoactive perovskite phases *via* temperature effects is therefore unlikely and the powder is expected to occur in its room temperature stable crystallographic state. Indeed, X-ray diffraction indicates that powders prepared with iodine contents above $x > 0.67$ preferentially crystallize in the photoinactive hexagonal phase, while powders with iodine contents $x < 0.67$ appear mostly in one of the photoactive phases. This effect also becomes evident from the visual appearance of the powders and their color change when changing the iodine content (see Fig. S2 in the ESI†). The addition of bromine into the perovskite lattice is known to stabilize the photoactive phase at room temperature particularly for iodine contents $x < 0.50$.[49]

While the crystallographic and phase properties of the mechano-chemically synthesized powder follow expected trends, properties of the resulting thin films are determined by the exact deposition approach as well as the film formation processes on the substrate and are therefore expected to deviate from the powder's characteristics. In fact, an outstanding characteristic of the herein developed CFS approach is the fact that independent of the actual composition (*i.e.*, the iodine-to-bromine ratio) all as-prepared thin films after flash sublimation exhibit a rather pure photoactive phase composition without significant amounts of crystalline photoinactive phases (see Fig. 3c). This is in stark contrast to previous attempts of single-source vapor processing of inorganic halide perovskite materials. For example, Igual-Muñoz *et al.* attempted to deposit $CsPb(I_{0.67}Br_{0.33})_3$ from a pre-synthesized powder in a single-source approach but failed to fabricate thin films in the desired photoactive phase.[36] It is believed that in their work an actual flash sublimation regime could not be achieved, resulting in a selective evaporation of the individual powder constituents and thus the formation of a highly disordered off-stoichiometric thin-film composition. In agreement with theoretical diffraction peak positions reported in previous works,[53,55] thin films prepared by CFS appear to crystallize in the photoactive orthorhombic (γ) phase. Increasing the bromine content shifts the peak position to higher diffraction angles as expected for a substitutional solid solution (see Fig. S5 in the ESI†) and agrees well with the linear shift of the bandgap previously noted. Peak positions for all iodine-to-bromine ratios are close to their theoretically expected values, indicating no major phase changes when varying the composition. However, a pronounced effect of the composition on the preferred crystallographic orientation is observed in thin films prepared by CFS. Increasing the bromine content continuously shifts the thin-film texture from a preferred (110) orientation to a more pronounced (020) orientation (see Fig. S5 in the ESI†). While it is obvious that this observation is directly linked to the iodine-to-bromine ratio in the thin film, the processes related to its emergence as well as its consequences on the opto-electronic properties of the thin films require further detailed investigations that go beyond the scope of this work.

Despite the already good crystallographic properties of the as-prepared inorganic halide perovskite thin films prepared by CFS, a short post-annealing step (at temperatures >300 °C) has been shown to be necessary for the achievement of high opto-electronic quality. In fact, solar cells employing absorbers that did not undergo a post-annealing typically show a significant deficit in performance (see Fig. S6 in the ESI†). In addition, charge carrier lifetimes improve by an order of magnitude during the post-annealing step indicating a significant improvement in the opto-electronic properties (see Fig. S7 in the ESI†). It should be noted that annealing for one minute is sufficient to improve film quality (see Fig. S8 and S9 in the ESI†), which does not increase the overall processing time significantly. The processes involved during the post-annealing step are complex since they cover structural, morphological, and chemical processes at the same time, thus, will only be broached shortly here. First and foremost, the annealing step results in an improvement in crystallographic quality obvious from the increase in intensity of the dominant diffraction peaks (see Fig. 3c). The improved crystallographic properties as well as the improved charge carrier lifetimes can directly be linked to a grain coarsening that is observed for all thin films independent of their exact iodine-to-bromine ratio (see Fig. 4). A particularly strong grain coarsening is observed for thin films with iodine contents $x > 0.45$ with the formation of grains with lateral dimensions of up to 500 nm, whereas thin films with iodine contents $x < 0.45$ undergo only a minor grain coarsening albeit grain morphology is also changing notably for these compositions. The driving force for the grain coarsening is believed to be lattice expansions and relaxations because of the changing crystallographic phase during annealing. While thin films with iodine contents $x < 0.67$ are expected to undergo only phase changes between different photoactive phases (*i.e.*, α, β, and γ phases) when heated up from room temperature to temperatures above 300 °C, thin films with iodine contents $x > 0.67$ can also convert into the photoinactive phase (*i.e.*, δ phase) before changing over to photoactive phases

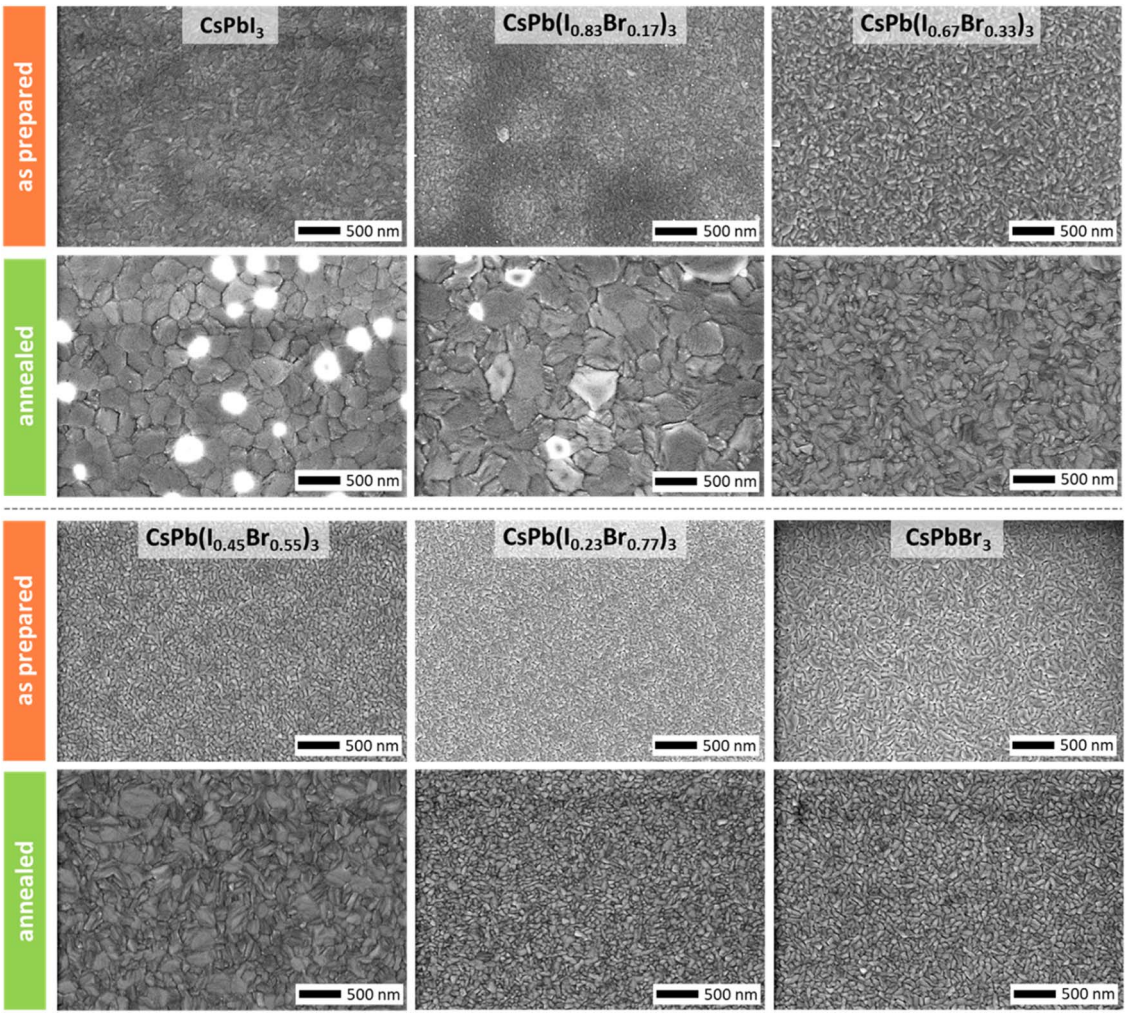

Fig. 4 Influence of the post-annealing step on the morphological properties of thin films with different iodine-to-bromine ratios prepared by CFS. Depending on the exact composition, a strong grain coarsening effect is observed. Samples were deposited on top of glass/ITO/SnO_2 and all images were taken with the same magnification.

at higher temperatures again.[52] In fact, for pure iodine samples ($x = 1.00$) and iodine-rich samples ($x = 0.83$) a full and partial conversion into the yellow photoinactive phase, respectively, is visually observable during annealing before the films convert back into a black photoactive phase. The transition into the photoinactive phase is expected to induce significant stress to the lattice, whose relaxation during reconversion into the photoactive phase is believed to result in a significant reorganization of the lattice and thus a significantly stronger grain coarsening effect. For the iodine-rich compositions that show this significant lattice reorganization, we also note the inclusion of bright spots in the SEM images typically associated with charging due to the insulating nature of the material. Attempts to identify this material have been unsuccessful although we postulate that they are either the orthorhombic phase (non-photoactive) or excess lead or cesium salts that have been expelled from the lattice. In either case, the total volume of the charging material must be small as all of the possible materials are crystalline and yet they produce no discernible peaks in the XRD patterns. Next to the apparent grain coarsening effect, a slight shift in diffraction peak position toward higher diffraction angles is observed for all thin-film compositions after annealing (see Fig. S5 in the ESI†). Given the fact that the shift in peak position is also observed for pure iodine and pure bromine samples the shift is likely not related to a change in composition or reorganization of iodine and bromine atoms within the lattice, but to a global effect that shifts all diffraction peaks by the same extent. Possible explanations could be the (partial) transition to a crystallographic phase with a larger volume (*i.e.*, tetragonal and/or cubic phases) and/or the formation of tensile strain or the relaxation of compressive strain. Interestingly, strongest peak shifts are observed for thin films that also exhibit largest grain sizes after annealing, which indicates a direct connection between the effect of grain coarsening and diffraction peak shift.

Efficient inorganic halide perovskite solar cells by continuous flash sublimation

Having discussed the general processes taking place during the deposition and thin-film formation of inorganic halide

perovskite materials prepared by CFS, their high quality – even at significantly higher deposition rates compared to previous approaches – is illustrated next by integrating these thin films into solar cells. As a testbed for the absorber fabrication, material compositions between $CsPb(I_{0.83}Br_{0.17})_3$ and $CsPb(I_{0.67}Br_{0.33})_3$ (commonly known as $CsPbI_2Br$) are chosen given their decent crystallographic phase stability together with the high number of previous studies both for solution-based and vapor-based deposition approaches allowing for direct comparison of the absorber quality. In this work, absorbers prepared by CFS are integrated into the layer stack sequence glass/ITO/SnO_2/absorber/spiro-MeOTAD/Au (see Fig. 5a), which is by far the most employed layer stack sequence in literature for similar absorber compositions, therefore allowing a direct comparison of the device performance despite the alternative absorber deposition method. However, it should be noted that spiro-MeOTAD is not considered an optimal choice given the mismatch of its highest occupied molecular orbital (HOMO) and the valence band of the absorber. In accordance with the previous discussion (see Fig. 4), the absorber consists of grains with lateral grain sizes of around 200 nm forming a fairly compact absorber layer principally comprised of individual columnar grains that span the complete absorber layer. However, a number of horizontal grain boundaries are observed that might have a limiting effect on device performance. Champion solar cells employing $CsPb(I_{0.83}Br_{0.17})_3$ absorbers (bandgap energy $E_g = 1.84$ eV) prepared by CFS achieve power conversion efficiencies (PCE) as high as 14.9%, open-circuit voltages (V_{oc}) of 1.17 V, fill factors (FF) of 76.0%, and short-circuit current densities (J_{sc}) of 16.8 mA cm^{-2} in reverse scan direction with a notable hysteresis in the fill factor resulting in forward scan direction values of PCE = 10.3%, V_{oc} = 1.12 V, FF = 55.1%, and J_{sc} = 16.7 mA cm^{-2} (see Fig. 5b). The PCE extracted from the reverse scan direction is synonymous to 57.8% of the theoretical detailed-balance limit and mostly limited by the open-circuit voltage (see Fig. S10 in the ESI†), which is a common issue for these material systems and in agreement with their limited charge carrier lifetimes (see Fig. S7 in the ESI†).[56–58] These achievements are not only a significant boost for inorganic solar cell absorbers prepared by single-source sublimation with a previous champion PCE of 9.0%,[33] but most importantly also result in the currently most efficient inorganic solar cell employing a vapor processed absorber (see Fig. 1 and Table S2 in the ESI†), surpassing the previous champion PCE of 13.0% significantly.[35] In addition, a good reproducibility is achieved with all solar cells fabricated in four individual evaporation processes outperforming the previous champion solar cells (see Fig. S11 in the ESI†). It is worth noting that similar performance is also achieved for absorbers with even higher bandgap energies up to 1.94 eV (see Fig. S12 in the ESI†). While the focus of this work is primarily on the fabrication of the absorber, a fully vapor processed device architecture is desirable to reduce complexity of the fabrication from an industrial point of view. As a proof of principle for a more practical layer stack, the second most efficient solar cell employing a vapor processed inorganic perovskite absorber in inverted architecture is realized when integrating these absorbers in a layer stack employing only vapor processed charge transport layers (see Fig. S13 in the ESI†). The observed hysteresis in devices in standard architecture is often attributed to issues at the interface between the absorber and spiro-MeOTAD (*e.g.*, a mismatch in band alignment) and the doping of the spiro-MeOTAD itself.[59–62] In fact, hysteresis disappears nearly completely if spiro-MeOTAD is replaced by an alternative hole transport material (*e.g.*, PDCBT) while its extent is further increased if the oxygen doping is replaced by a cobalt doping (see Fig. S14 in the ESI†). Furthermore, the addition of a thin C_{60} fullerene interface layer on top of the SnO_2 electron transport layer, which has been reported to lower hysteresis in the co-evaporation of hybrid perovskite materials,[63–66] is not able to reduce hysteresis in this case, confirming that the issue is at the hole extraction side (see Fig. S15 in the ESI†).[67] The development of more suitable hole transport materials next to spiro-MeOTAD, as well as alternative device architectures, are believed to be crucial for the further development of inorganic perovskite solar cells as they may not only remove hysteresis

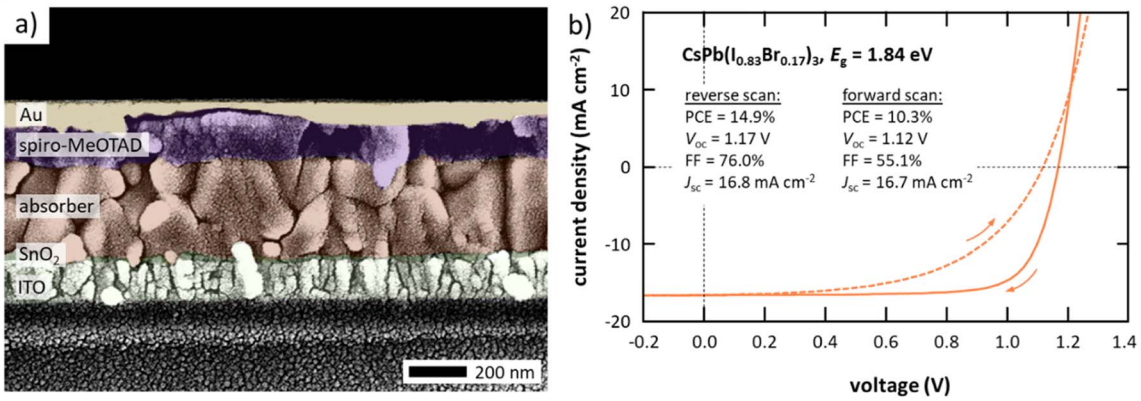

Fig. 5 Fabrication of state-of-the-art inorganic halide perovskite solar cells by CFS. (a) Layer stack sequence of the solar cells fabricated in this work (glass/ITO/SnO_2/absorber/spiro-MeOTAD/Au). (b) *J*–*V* scan in forward and reverse scan direction of the champion solar cell employing a $CsPb(I_{0.83}Br_{0.17})_3$ absorber realized in this work.

effects but also lift open-circuit voltages closer to their theoretical values. Despite the observed hysteresis a stable power output can be achieved when operating the devices at constant voltage for several minutes (see inset in Fig. S16 in the ESI†).

In addition to the stable power output, a good long-term shelf stability is observed for these devices (see Fig. 6). Over the course of two months an overall loss in performance of around 10%rel is observed, being in line with typical stability properties achieved in literature.[41,62,68–70] Most importantly, the loss in performance is primarily attributed to a loss in fill factor, whereas both short-circuit current density and open-circuit voltage are less affected, indicating a good overall phase stability in these devices. In fact, good phase stability in thin films prepared by CFS, compared to a solution processed thin film, is proven visually based on the significantly improved resistivity against phase change when exposed to ambient conditions for several hours (see Fig. S17 in the ESI†). It is believed that the small-crystalline grain structure of the flash sublimed thin films (see Fig. 4 and 5a), and their homogeneous and phase pure composition (see Fig. S1† and 3c), are the main reasons for the improved phase stability observed when exposed to ambient conditions. Similar morphology and phase related aspects have been reported before to have a crucial influence on the phase stability of inorganic perovskite materials.[71–75] Furthermore, the observed loss in fill factor when stored in inert environment for prolonged time is in large part reversible by improving the contact resistance (by improving the electrical contact at the metal electrodes with silver paste) as well as by enhancing doping of spiro-MeOTAD (by reoxidatizing of the spiro-MeOTAD for 24 h) after the long-term measurement, again highlighting the need for the development of alternative hole transport materials.

The high quality of inorganic halide perovskite absorbers fabricated by CFS is particularly outstanding when considering the significantly higher deposition rates, thus reduced processing times, compared to previously reported approaches (see Fig. 7a and Table S3 in the ESI†). The herein developed process is capable of typical deposition rates in the range of 67 nm min^{-1} to 134 nm min^{-1} being the first efficient vapor deposition approach for inorganic halide perovskite materials surpassing deposition rates of 100 nm min^{-1}, while at the same time being nearly four times faster than the fastest vapor deposition process for inorganic halide perovskites reported before.[76] Most importantly, absorbers prepared by CFS are fabricated up to 45 times faster than by both the currently most efficient single-source evaporation process as well as the process resulting in the most efficient vapor processed inorganic halide perovskite solar cells, however, at the same time also outperforming these previous results clearly.[33,35] It is worth noting that absorbers prepared by CFS in the herein investigated deposition rate regime show a rather low dependency on the actual deposition rate and PCEs above 14% are achieved both for deposition rates as low as 66 nm min^{-1} and as high as 127 nm min^{-1} (see Table S3 in the ESI†). As a practical comparison, First Solar, Inc. deposits their Cd(Se,Te) absorbers at rates near 10 000 nm min^{-1} using vapor transport deposition.[6,77] Next to limited processing times of established vapor-based processes, a successful implementation in an industrial environment of a majority of these approaches are also limited due their lack of continuous deposition. Particularly, vapor processes employing organic compounds that are in prolonged contact with a hot evaporation source have been reported to be problematic given the notable degradation of the organic molecules.[78,79] Other approaches specifically designed to be faster than established processes like single-source approaches with pre-coated evaporation boats are batch processes *per se*. Given the fact that the pre-synthesized powder in the CFS approach is never in contact with heat before it reaches the actual evaporation boat, it is an excellent candidate for a continuous deposition. As a matter of fact, good reproducibility is achieved when CFS is operated continuously, which is demonstrated here based on solar cells that are fabricated in five consecutive evaporation runs in which only the substrates are replaced in between runs while the same source powder is used for all five runs (see Fig. 7b). Variations in PCE between individual runs stay within a reasonable level with the mean values of PCE varying only by about $\pm 5\%_{rel}$, which is comparable with the overall reproducibility of the process (see Fig. S11 in the ESI†). The main cause for these variations is related to variations in fill factor, which is again linked here to challenges at the interface between absorber and spiro-MeOTAD. Overall, the key features of the herein developed approach, namely its continuous deposition and the compared with established vapor-based deposition process orders of magnitude faster deposition rates, together with the significant improvement in performance of inorganic halide perovskite solar cells compared to previous reports make the CFS approach an outstandingly promising candidate for further research and development – not only in a laboratory environment but also for a potential transfer toward an industrial application. Nevertheless, it needs to be noted that the herein employed setup does not allow a completely continuous operation as regular

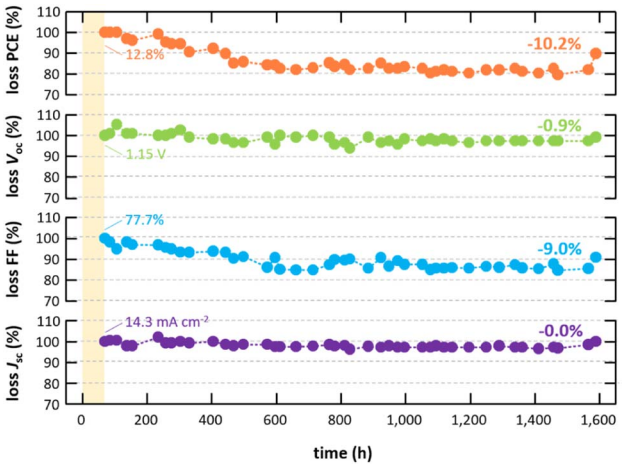

Fig. 6 Shelf-time stability of a solar cell employing a $CsPb(I_{0.67}Br_{0.33})_3$ absorber prepared by CFS with an oxygen-doped spiro-MeOTAD hole transport layer. Trends in solar cell parameters during storage in nitrogen over the course of two months. The solar cell underwent an oxidation step in ambient air (relative humidity < 20%) for 70 h before the start of the measurement (highlighted in yellow).

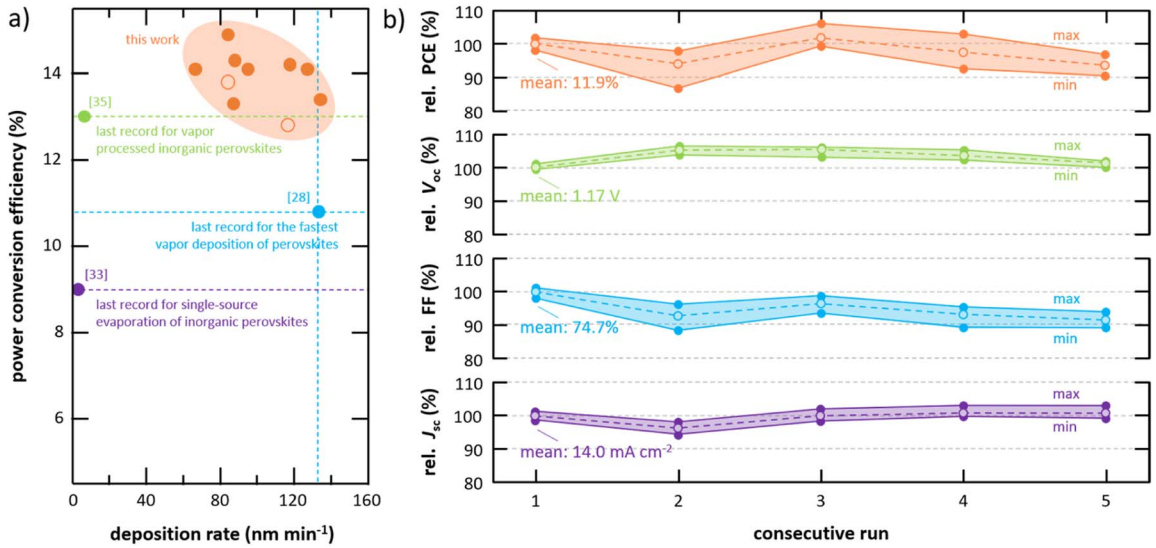

Fig. 7 Deposition rate and continuous deposition of the CFS approach. (a) Influence of the deposition rate on the performance of solar cells employing a $CsPb(I_{0.83}Br_{0.17})_3$ absorber prepared by CFS. Open symbols indicate solar cells employing absorber compositions with higher bromine ratios. Recent record values for vapor processed perovskite solar cells from literature were highlighted. (b) Performance of solar cells with a $CsPb(I_{0.67}Br_{0.33})_3$ absorber prepared with continuous deposition in five consecutive evaporation runs. Filled symbols indicate maximum and minimum values, open symbols mean values of the *J*–*V* parameters extracted from the reverse scans of 12 solar cells for each run. All solar cells were prepared without replacing the source powder in between runs.

refilling of the powder is required given the limited powder reservoir volume. Suitable in-line feeding systems or sufficiently large powder reservoirs have to be implemented to make this approach truly applicable in an industrial setting.

Outlook: loss mitigation strategies for flash sublimed inorganic halide perovskites

While the previous discussions have demonstrated the high quality of the herein developed flash sublimation technique compared to previously reported vapor-based approaches, significant improvements in the open-circuit voltage are required to be able to compete with state-of-the-art perovskite solar cell materials. In the following, photoluminescence quantum yield (PLQY) measurements are performed to gain further insights into the dominant loss paths in the layer stack sequence employed in this work as well as to propose directions for future research.[80–84] To determine the most limiting layers in the device stack, inorganic perovskite absorbers with different bandgap energies between 1.8 eV and 2.2 eV in two different layer stack sequences are investigated here: (1) a device stack with just the absorber and electron extraction layer (glass/SnO_2/absorber) that enables insights into absorber related limitations as well as potential non-radiative recombination at the electron extracting layer and (2) the full device stack (glass/ITO/SnO_2/absorber/spiro-MeOTAD/Au) to gain further insights into the effect of the hole extracting layer. An investigation of the uncontacted absorber could not be performed in this work as significantly different growth behavior of the absorbers were observed on glass and glass/ITO/SnO_2. However, previous investigations on solution processed inorganic halide perovskites have indicated a rather high defect tolerance of the interface between absorber and electron extracting layer and in turn related losses in the quasi-Fermi level splitting (being a direct measure for the open-circuit voltage of a device) of only around 50 meV.[84] Similar to previous reports, the absolute PLQY of these materials is rather low, ranging between 7×10^{-4} and 7×10^{-3} at one sun intensity. In spite of these low yields, the measurements can still be used to extract the quasi-Fermi level splitting (QFLS) for each measurement. Comparing the quasi-Fermi level splitting of these two layer stack sequences with different absorber bandgap energies emphasizes non-radiative recombination inside the absorber to be the main limitation of the observed deficit in open-circuit voltage (see Fig. 8). Losses in the quasi-Fermi level splitting ΔQFLS between 250 meV and 350 meV at one sun intensity are observed for the absorber (green-colored lines and data points) when compared to the detailed-balance limit (orange-colored lines) of the respective bandgap energies, which are comparable to similar absorber compositions prepared *via* solution-based approaches.[84] Non-radiative, trap-assisted Shockley-Read-Hall recombination is believed to be a primary origin of this loss as deduced from the slight reduction of the quasi-Fermi level splitting deficit ΔQFLS with increasing light intensity, which is in agreement with the rather low charge carrier lifetimes observed in these films (see Fig. S7 in the ESI†). In that regard, grain boundaries and correlated strain related effects are believed to play a particular role in the limitation of the absorber quality. In fact, it is observed that the absorber related deficit is significantly worse for wider bandgap absorber compositions ($x < 0.83$) that were identified to undergo only a minor grain coarsening effect during the post-annealing step (see Fig. 4) and in turn are prone to a significantly higher density of grain boundaries. Lowering the density of grain boundaries in the absorber by improving

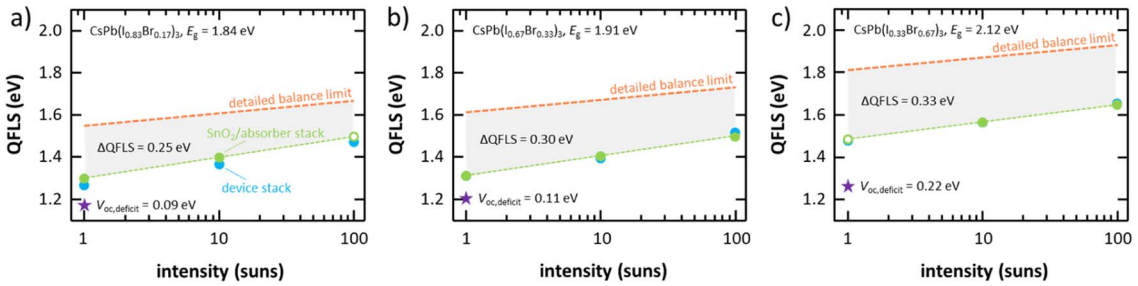

Fig. 8 Intensity dependent photoluminescence quantum yield (PLQY) investigations on solar cells employing a $CsPb(I_{0.83}Br_{0.17})_3$ (a), $CsPb(I_{0.67}Br_{0.33})_3$ (b), or $CsPb(I_{0.33}Br_{0.67})_3$ (c) absorber prepared by CFS. Filled symbols are measured values, open symbols could not be extracted due to too weak signals and have been linearly extrapolated based on measured data points. Purple star symbols indicate the open-circuit voltage values that were extracted from *J*–*V*-measurements.

the quality of film formation is believed to play a crucial role in lowering this deficit. The discussion before has shown that the fast deposition of the herein developed process inevitably results in a rather small crystalline grain structure (see Fig. 4). Additives in the powder counteracting the high density of nuclei in the initial stage of film formation, the addition of heat to the substrate during the deposition to assist grain coarsening directly in the film growth process, as well as the investigation of alternative substrate materials that influence grain growth (*e.g.*, *via* quasi-epitaxial growth modes) are believed to be promising approaches to overcome these limitations.

While for hybrid organic–inorganic perovskite materials the choice of the hole extracting layer does have a significant impact on the quasi-Fermi level splitting,[81,85,86] the addition of the spiro-MeOTAD hole extracting layer (and both electrodes) to the flash sublimed absorber does not result in a significant enhancement of non-radiative recombination losses (orange-colored lines) – independently of the respective absorber bandgap energy. This again highlights the limited absorber bulk quality to be the main bottleneck of the current device architecture. Nevertheless, the improper choice of spiro-MeOTAD as the hole extracting layer is responsible for an additional loss in the maximum extractable open-circuit voltage. Comparing the optically extracted open-circuit voltage of the completed devices (blue-colored data points) and the actually measured open-circuit voltage of the devices (purple star symbols) reveals an additional loss $V_{oc,deficit}$ between 90 meV and 250 meV at one sun intensity that increases with increasing bandgap energy of the absorber. This second most serious loss in the layer stack can directly be related to the bandgap mismatches between the highest occupied molecular orbital of the hole extraction layer and the valence band of the absorber.[81] As already discussed before, the investigation of alternative hole selective materials is believed to play a crucial role to overcome this limitation and is considered of particular relevance not only for the herein investigated flash-sublimed absorbers but for the advancement of inorganic halide perovskite materials in general.

Conclusion

In this work, continuous flash sublimation (CFS) is introduced as a novel and promising approach for the fabrication of high-quality inorganic halide perovskite materials. With demonstrated power conversion efficiencies of 15%, the approach does not only result in the currently most efficient vapor processed solar cells employing an inorganic halide perovskite absorber, but at the same time solves two of the most urgent challenges of vapor processed perovskite solar cells: the significantly too long processing times and the lack of continuous deposition, both of which hamper a swift application of vapor-based approaches on an industrial scale. With deposition rates as high as 134 nm min^{-1}, the herein developed process outperforms any previously reported vapor-based deposition approach in terms of deposition rates, while at the same maintaining or even improving device performance – also in continuous deposition. Beside the progress from a performance and throughput point of view, continuous flash sublimation is shown to enable simple access to high-quality photoactive $CsPb(I_xBr_{1-x})_3$ thin films of arbitrary composition and good phase stability without major changes to the process, being a significant advantage compared to more complex solution-based approaches. Finally, the simplicity of the developed process with its reduction to three simple process steps reduces the number of process parameters and in turn demands for process control and monitoring, enabling a good overall reproducibility. Based on detailed photoluminescence quantum yield (PLQY) measurements the limited charge carrier lifetimes and overall performance of flash-sublimed perovskite solar cells is linked to deficits of the absorber layer itself that significantly lower the extractable open-circuit voltages. The development of more suitable selective contact materials for the wide-bandgap materials as well as a fine-tuning of the film growth mechanisms are believed to play a particular role in lowering hysteresis as well as boosting both performance and long-term stability of inorganic halide perovskite absorbers closer to those of their hybrid organic–inorganic counterparts. Finally, efforts toward better fully vapor processed layer stack sequences are believed to create additional advantages from an industrial point of view.

Experimental section

Materials and process environment

All materials used in this work were used as received from the suppliers. Glass substrates with pre-patterned indium tin oxide

(ITO, CAS: 50926-11-9) were obtained from Colorado Concept Coatings LLC. The commercial tin oxide (SnO_2) colloidal dispersion (15 wt% dispersion, CAS: 18282-10-5) was purchased from Alfa Aesar. Lead iodide (PbI_2, 99.999% purity, ultra-dry, CAS: 10101-63-0), lead bromide ($PbBr_2$, 99.999% purity, ultra-dry, CAS: 10031-22-8), cesium iodide (CsI, 99.999% purity, CAS: 7789-17-5), and cesium bromide (CsBr, 99.999% purity, CAS: 7787-69-1) were purchased from Alfa Aesar. The hole transport material 2,2″,7,7″-tetrakis[*N*,*N*-di(4-methoxyphenyl) amino]-9,9′-spirobifluorene (spiro-MeOTAD, > 99.8% purity, CAS: 207739-72-8) was obtained from the Luminescence Technology Corporation, its dopants bis(trifluoromethane)sulfonimide lithium salt (Li-TFSI, 99.95% purity, CAS: 90076-65-6) and 4-*tert*-butylpyridine (98% purity, CAS: 3978-81-2) as well as the solvents chlorobenzene (99.8%, anhydrous, CAS: 108-90-7) and acetonitrile (99.8%, anhydrous, CAS: 75-05-8) from Sigma-Aldrich. All experiments in this work were performed in Golden, Colorado, USA at an altitude of 1730 m. The temperature was between 20 °C and 25 °C while relative humidity was typically below 40%. Samples and materials were stored in inert atmosphere if not stated otherwise.

Inorganic halide perovskite powder preparation

Source powders for the flash sublimation of the inorganic halide perovskite thin films were prepared *via* a mechanochemical synthesis (ball milling). For this, the individual powder constituents PbI_2, $PbBr_2$, CsI, and CsBr were weighed out into a Teflon® canister with a stoichiometric ratio depending on the iodine-to-bromine ratio inside a nitrogen-filled glovebox. A small PbI_2 excess of 5% (mass percentage) has been shown to be beneficial for the performance of the absorbers. For all powders with an iodine content between $0.45 \leq x \leq 0.83$ $PbBr_2$ was used as the only bromine source. For example, 0.800 g PbI_2, 0.637 g $PbBr_2$, and 0.902 g CsI were mixed for a powder with the composition $CsPb(I_{0.67}Br_{0.33})_3$. The powder constituents were manually pre-mixed and alumina (Al_2O_3) balls with a diameter of around 5 mm added to the powder. Afterward, the canister was sealed, transferred outside the glovebox, and mixed in a SPEX SamplePrep 8000M mixer for 20 min. Right after the mixing, the canister was transferred back into inert atmosphere, opened, and the powder sifted in a sieve with a 250 μm mesh width, ensuring a consistent and reproducible feeding of the powder (see ESI† section Notes on CFS and powder preparation). Depending on the iodine-to-bromine ratio the powders showed a clear color change that indicates a reaction into perovskite during the mixing process (see Fig. S2 in the ESI†). The powder was stored in inert atmosphere until usage.

Substrate preparation

Glass substrates coated with (pre-patterned) indium tin oxide (ITO) were cleaned in acetone and isopropanol in an ultrasonic bath for 15 min each, followed by an additional cleaning step in ozone for 15 min immediately before the deposition of the electron transport layers. As electron transport layer solution processed tin dioxide (SnO_2) in nanoparticular form was employed. For this, one volume part of the commercial SnO_2 colloidal dispersion was diluted with four parts of deionized water to a concentration of 3 wt%. The deposition on top of the ITO front electrode was performed by spin coating at 3000 rpm for 30 s followed by an annealing step at 150 °C for 30 min in ambient air. Right before the deposition of the absorber layer, the substrates were again treated in ozone for 15 min. For samples used for optical characterization, bare glass substrates that were cleaned in acetone, isopropanol, and ozone were used.

Inorganic halide perovskite deposition

The deposition of the inorganic halide thin films by continuous flash sublimation (CFS) was performed in a strongly modified Edwards AUTO 306 bell jar evaporator (see Fig. 2 for a scheme of the system). The system was equipped with a home-made vibratory feeder driven by an electromagnet *via* an A/C sine wave. The sine wave was generated *via* a BK PRECISION waveform generator. Typical voltage amplitudes and frequencies of the sinusoidal output signal during operation were 1.5 V and 40 Hz to 60 Hz, respectively. The vibratory feeder was equipped with a powder reservoir providing space for about 3 g of presynthesized powder. After moving along a PTFE trough, the powder fell into a funnel equipped with an additional stainless-steel mesh and then into a quartz glass tube connected to a baffled tantalum evaporation boat. The evaporation boat was purchased from the RD Mathis company (product number: SB-6) and equipped with a custom-made lid with additional openings on the opposite side of the powder entrance. Baffles inside the boat as well as a sufficient distance between powder entrance and vapor exit guaranteed a sufficient thermal exposure of the powder and thus a complete sublimation. The boat lid prevented spitting, while the funnel and tube kept the powder from spilling. It was recognized that adequate sealing between the evaporation boat and the quartz glass tube on the entrance side of the evaporation boat lid was particularly important to prevent flash sublimation into the wrong direction and to achieve sufficient sublimation yield. Thus, an additional ceramic plug was designed that did not only properly seal the area between quartz glass tube and boat lid but also helped to prevent clogging of the quartz glass tube during deposition given its non-negligible thermal conductivity. Surface temperature of the evaporation boat during the deposition was measured right at the point of powder entry by means of a type K thermocouple and was in the range of 600 °C to 700 °C (equivalent to a boat current between 90 A and 120 A), although the bright orange-glowing boat indicated temperatures between 900 °C and 1100 °C. Base pressures before the evaporation were in the range of $<1.5 \times 10^{-5}$ mbar and stayed rather unchanged during deposition. Typical deposition times for a 350 nm thick thin film ranged from 2 min to 5 min equivalent to a powder supply rate between 40 mg min^{-1} and 100 mg min^{-1}, which was adjusted *via* the frequency of the vibratory feeder. During the process, the substrates were rotating but not actively cooled nor heated. The distance between evaporation boat and substrates was kept constant at a value of around 15 cm. Right after the

deposition, the evaporator was vented to air, the thin films were transferred into a nitrogen-filled glovebox, and annealed at a temperature of 330 °C (380 °C for thin films with iodine contents $x < 0.67$) for 0.5 min to 1 min.

Solar cell fabrication

Solar cells in this work were fabricated with the layer stack sequence glass/ITO/SnO_2/absorber/spiro-MeOTAD/Au. Absorber thicknesses typically of 350 nm were used in this work. The hole transport layer spiro-MeOTAD was deposited by spin coating a solution at 3000 rpm for 30 s in a nitrogen-filled glovebox without subsequent annealing. For the oxygen doped spiro-MeOTAD solution, 73 mg spiro-MeOTAD were dissolved in 1 ml chlorobenzene and 35 μl of a Li-TFSI solution (260 mg in 1 ml acetonitrile) and 30 μl of 4-*tert*-butylpyridine added. After the deposition of the hole transport layer the samples were stored in dry ambient atmosphere for typically 36 h. For the cobalt-doped spiro-MeOTAD solution, 71 mg spiro-MeOTAD were dissolved in 1 ml chlorobenzene and 17.5 μl of a Li-TFSI solution (520 mg in 1 ml acetonitrile), 29 μl of a Co-TFSI solution (300 mg in 1 ml acetonitrile), and 29 μl of 4-*tert*-butylpyridine added. The spiro-MeOTAD solutions were always prepared freshly right before the deposition. Finally, the devices were equipped with a 100 nm thick gold rear electrode deposited by thermal evaporation through a shadow mask (0.12 cm^2) at an evaporation rate of 2 Å s^{-1} in an Angstrom Engineering Inc. evaporator.

Characterization

Current-density–voltage (*J–V*) characteristics were measured in a solar simulator with a xenon lamp (Newport Oriel 94043A) under AM1.5G spectra (100 mW cm^{-2}) in both forward and reverse scan direction at a scan speed of <0.5 V s^{-1}. The intensity was calibrated with a silicon reference solar cell equipped with a KG5 band pass filter. In addition, intensity of the lamp was regularly calibrated against NREL's solar simulator used for official certification purposes. During the measurement, the temperature of the solar cells was not actively controlled, which results in a slight underestimation of the open-circuit voltage (*ca.* 30 mV) as well as the power conversion efficiency. The active device area during measurement was defined with a shadow mask to be 0.06 cm^2. For X-ray diffraction (XRD) investigations, a Rigaku SmartLab 3kW system with (non-filtered) Cu K_α radiation was used, and measurements were performed in Bragg–Brentano configuration in ambient environment. Scanning electron microscope (SEM) investigations were carried out in a Hitachi S-4800 scanning electron microscope with secondary electron detector and a primary electron energy of 3 keV. For cross-sectional investigations the cross sections were covered with a few nanometers thick chromium layer deposited by sputtering to prevent charging. Samples for both XRD and SEM were deposited on top of glass/ITO/SnO_2 substrates. Transmittance and reflectance were measured in an Agilent Cary 7000 spectrophotometer in ambient environment. For both optical measurements the film side of the sample was faced toward the incident light beam. For the calculation of the absorption coefficient and the Tauc plots, absorptance was calculated using the formula $A = 1 - T - R$ and the substrate background subtracted from the measured absorptance using previously reported methods.[87] Thickness of the thin films was determined in a Veeco DEKTAK 8 stylus profilometer. Surface images were taken in a Nikon Eclipse LV100 optical microscope. Transient photoluminescence (TRPL) measurements were performed in a home-made measurement setup employing a pulsed laser diode and a time-correlated single photon counting unit from PicoQuant. A laser with a wavelength of 405 nm, a repetition rate of 1 MHz, and a measured power at the sample surface of <15 μW was used. Photoluminescence mapping was conducted in a home-made setup employing a Princeton Instruments PIXIS Silicon CCD camera with 600 nm long pass filter. The large-area samples were excited by a scanning laser with a wavelength of 532 nm and a power of 1 mW on an area of 1 × 1 mm^2. Photoluminescence quantum yield (PLQY) measurements were obtained *via* integration of absolute intensity photoluminescence (AIPL) spectra.[81] The spectra were acquired using a modified Horiba LabRAM HR-800, a 532 nm laser diode excitation source, and a 10× objective lens (NA = 0.25) for illumination and emission collection. An 800 μm in diameter confocal hole was used for all measurements. A 150 g mm^{-1} Czerny–Turner monochromator blazed at 500 nm was used to spectrally resolve the luminescence, after which the emitted light was passed to a Si CCD array detector. An Oriel optical power meter and Thorlabs beam profiler were used to calibrate the photon flux, which was set to the desired number of equivalent suns according to the integration of the AM1.5 solar spectrum above the bandgap of the respective absorber material. The photon detection was calibrated using a blackbody source (IR-301, Infrared Systems Development) at 1050 °C with 10 μm pinhole. All confocal PLQY experiments were conducted in a nitrogen filled container sealed with an O-ring and vacuum grease with a quartz window to prevent oxygen and moisture exposure. Composition of the samples was determined by inductively coupled plasma mass spectrometry (ICP-MS) using an Agilent 7700 system with ASX-500 autosampler. Two 1" × 1" glass slides were prepared for each analysis. One slide was dissolved in 2% nitric acid (HNO_3) and 50 ng ml^{-1} yttrium (yttrium as an internal standard), the second slide was dissolved in a solution of 1 wt% triethanolamine (0.1 wt% ethylenediaminetetraacetic acid (EDTA) and 50 ng ml^{-1} yttrium). For both samples the solution was further diluted to a target concentration of 20 ng ml^{-1} to 100 ng ml^{-1}. Samples in the acid matrix were used to detect cesium and lead, base matrix samples were used to detect cesium, iodine, and bromine. Final stoichiometry was determined by using the cesium concentration in both samples to connect the lead to halide ratios.

Conflicts of interest

There are no conflicts to declare.

Acknowledgements

The work was authored in part by the National Renewable Energy Laboratory, operated by Alliance for Sustainable Energy,

LLC, for the US Department of Energy (DOE) under contract no. DE-AC36-08GO28308. David Moore was supported by the U.S. Department of Energy Office of Energy Efficiency and Renewable Energy (EERE) under the Solar Energy Technologies Office (SETO) "Advanced Perovskite Solar Cells and Modules" program (Agreement Number 38256), Tobias Abzheier was supported by SETO agreement number DE-EE0009017. Additional support for machine development was provided by NREL's Shell Game-Changer Award. The views expressed in the article do not necessarily represent the views of the DOE or the U.S. Government. The U.S. Government retains and the publisher, by accepting the article for publication, acknowledges that the U.S. Government retains a nonexclusive, paid-up, irrevocable, worldwide license to publish or reproduce the published form of this work, or allow others to do so, for U.S. Government purposes.

References

1 Z. Saki, M. M. Byranvand, N. Taghavinia, M. Kedia and M. Saliba, Solution-processed perovskite thin-films: The journey from lab: The large-scale solar cells, *Energy Environ. Sci.*, 2021, **14**, 5690–5722.
2 T. D. Siegler, *et al.*, The Path to Perovskite Commercialization: A Perspective from the United States Solar Energy Technologies Office, *ACS Energy Lett.*, 2022, **7**, 1728–1734.
3 T. Bailey, Samsung Display Apparently Struggling with QD-OLED Production, 2022, available at: **https://www.whathifi.com/news/samsung-display-apparently-struggling-with-qd-oled-production**.
4 S. Kurtz, *et al.*, Historical Analysis of Champion Photovoltaic Module Efficiencies, *IEEE J. Photovolt.*, 2018, **8**, 363–372.
5 D. Feldman, *et al.*, *Spring 2022 Solar Industry Update*, 2022.
6 Powell, *R. C. Research Leading to High-Throughput Manufacturing of Thin-Film CdTe PV Modules*, 2006.
7 Heliatek GmbH, "State-of-the-art": Vacuum roll-to-roll production of organic solar film, 2022, available at: **https://www.heliatek.com/en/technology/roll-to-roll-series-production/**.
8 T. Abzieher, *et al.*, Vapor phase deposition of perovskite photovoltaics: short track to commercialization?, *Energy Environ. Sci.*, 2024, DOI: **10.1039/D3EE03273F**.
9 D. B. Ritzer, *et al.*, Upscaling of perovskite solar modules: The synergy of fully evaporated layer fabrication and all-laser-scribed interconnections, *Prog. Photovolt.: Res. Appl.*, 2022, **30**, 360–373.
10 T. Abzieher, *et al.*, Efficient All-Evaporated pin-Perovskite Solar Cells: A Promising Approach towards Industrial Large-Scale Fabrication, *IEEE J. Photovolt.*, 2019, **9**, 1249.
11 L. Gil-Escrig, *et al.*, Fully Vacuum-Processed Perovskite Solar Cells on Pyramidal Microtextures, *Sol. RRL*, 2021, **5**, 2000553.
12 X. Y. Chin, *et al.*, Interface passivation for 31.25%-efficient perovskite/silicon tandem solar cells, *Science*, 2023, **381**, 59–63.
13 J. Ávila, C. Momblona, P. P. Boix, M. Sessolo and H. J. Bolink, Vapor-Deposited Perovskites: The Route to High-Performance Solar Cell Production?, *Joule*, 2017, **1**, 431–442.
14 Y. Vaynzof, The Future of Perovskite Photovoltaics—Thermal Evaporation or Solution Processing?, *Adv. Energy Mater.*, 2020, **10**, 2003073.
15 Q. Guesnay, F. Sahli, C. Ballif and Q. Jeangros, Vapor deposition of metal halide perovskite thin films: Process control strategies to shape layer properties, *APL Mater.*, 2021, **9**, 100703.
16 H. Li, *et al.*, Sequential vacuum-evaporated perovskite solar cells with more than 24% efficiency, *Sci. Adv.*, 2022, **8**, eabo7422.
17 National Renewable Energy Laboratory (NREL), Best Research-Cell Efficiency Chart, 2024, available at: **https://www.nrel.gov/pv/cell-efficiency.html**.
18 M. M. Tavakoli, A. Simchi, X. Mo and Z. Fan, High-quality organohalide lead perovskite films fabricated by layer-by-layer alternating vacuum deposition for high efficiency photovoltaics, *Mater. Chem. Front.*, 2017, **1**, 1520–1525.
19 L. Luo, *et al.*, Large-area perovskite solar cells with CsxFA1−xPbI3−yBry thin films deposited by a vapor-solid reaction method, *J. Mater. Chem. A*, 2018, **6**, 21143–21148.
20 M. M. Tavakoli, P. Yadav, D. Prochowicz, R. Tavakoli and M. Saliba, Multilayer evaporation of MAFAPbI3-xClx for the fabrication of efficient and large-scale device Perovskite solar cells, *J. Phys. D Appl. Phys.*, 2019, **52**, 034005.
21 L. Qiu, *et al.*, Rapid hybrid chemical vapor deposition for efficient and hysteresis-free perovskite solar modules with an operation lifetime exceeding 800 hours, *J. Mater. Chem. A*, 2020, **8**, 23404–23412.
22 D. Lin, *et al.*, The selection strategy of ammonium-group organic salts in vapor deposited perovskites: From dimension regulation to passivation, *Nano Energy*, 2021, **84**, 105893.
23 L. Harris and B. M. Siegel, A method for the evaporation of alloys, *J. Appl. Phys.*, 1948, **19**, 739–741.
24 G. Longo, L. Gil-Escrig, M. J. Degen, M. Sessolo and H. J. Bolink, Perovskite solar cells prepared by flash evaporation, *Chem. Commun.*, 2015, **51**, 7376.
25 H. Xu, *et al.*, Grain growth study of perovskite thin films prepared by flash evaporation and its effect on solar cell performance, *RSC Adv.*, 2016, **6**, 48851–48857.
26 M. Tai, *et al.*, Laser-Induced Flash-Evaporation Printing CH3NH3PbI3 Thin Films for High-Performance Planar Solar Cells, *ACS Appl. Mater. Interfaces*, 2018, **10**, 26206–26212.
27 M. Tai, *et al.*, Efficient Inorganic Cesium Lead Mixed-Halide Perovskite Solar Cells Prepared by Flash-Evaporation Printing, *Energy Technol.*, 2019, **7**, 1800986.
28 P. Fan, *et al.*, High-performance perovskite CH3NH3PbI3 thin films for solar cells prepared by single-source physical vapour deposition, *Sci. Rep.*, 2016, **6**, 29910.
29 H. Peng, *et al.*, High-Quality Perovskite $CH_3NH_3PbI_3$ Thin Films for Solar Cells Prepared by Single-Source Thermal Evaporation Combined with Solvent Treatment, *Materials*, 2019, **12**, 1237.

30 Z. H. Zheng, *et al.*, Single Source Thermal Evaporation of Two-dimensional Perovskite Thin Films for Photovoltaic Applications, *Sci. Rep.*, 2019, **9**, 17422.
31 P. Fan, *et al.*, Single-Source Vapor-Deposited Cs2AgBiBr6 Thin Films for Lead-Free Perovskite Solar Cells, *Nanomaterials*, 2019, **9**, 1760.
32 J. Li, *et al.*, Fabrication of efficient CsPbBr3 perovskite solar cells by single-source thermal evaporation, *J. Alloys Compd.*, 2020, **818**, 152903.
33 M. H. Abib, *et al.*, Direct deposition of Sn-doped CsPbBr3perovskite for efficient solar cell application, *RSC Adv.*, 2021, **11**, 3380–3389.
34 L. Liu, S. E. Yang, P. Liu and Y. Chen, High-quality and full-coverage CsPbBr3 thin films *via* electron beam evaporation with post-annealing treatment for all-inorganic perovskite solar cells, *Sol. Energy*, 2022, **232**, 320–327.
35 H. Y. Lin, *et al.*, Efficient Cesium Lead Halide Perovskite Solar Cells through Alternative Thousand-Layer Rapid Deposition, *Adv. Funct. Mater.*, 2019, **29**, 1905163.
36 A. M. Igual-Muñoz, *et al.*, Room-Temperature Vacuum Deposition of CsPbI2Br Perovskite Films from Multiple Sources and Mixed Halide Precursors, *Chem. Mater.*, 2020, **32**, 8641–8652.
37 H. L. Hwang, C. C. Tu, J. S. Maa and C. Y. Sun, On the preparation of CuInS2 thin films by flash evaporation, *Sol. Energy Mater.*, 1980, **2**, 433–446.
38 S. Tan, *et al.*, Temperature-Reliable Low-Dimensional Perovskites Passivated Black-Phase CsPbI 3 toward Stable and Efficient Photovoltaics, *Angew. Chem.*, 2022, **134**, e202201300.
39 Z. Guo, *et al.*, VOC Over 1.4 V for Amorphous Tin-Oxide-Based Dopant-Free CsPbI2Br Perovskite Solar Cells, *J. Am. Chem. Soc.*, 2020, **142**, 9725–9734.
40 Y. Gao, *et al.*, Boosting Performance of CsPbI 3 Perovskite Solar Cells *via* the Synergy of Hydroiodic Acid and Deionized Water, *Adv. Energy Sustainability Res.*, 2022, **3**, 2100149.
41 W. Zhu, *et al.*, High-Efficiency (>14%) and Air-Stable Carbon-Based, All-Inorganic CsPbI2Br Perovskite Solar Cells through a Top-Seeded Growth Strategy, *ACS Energy Lett.*, 2021, **6**, 1500–1510.
42 W. Jeong, *et al.*, Unraveling the Antisolvent Bathing Effect on CsPbI 3 Crystallization under Ambient Conditions, *Adv. Funct. Mater.*, 2022, **32**, 2207342.
43 S. S. Mali, J. V. Patil and C. K. Hong, Hot-Air-Assisted Fully Air-Processed Barium Incorporated CsPbI2Br Perovskite Thin Films for Highly Efficient and Stable All-Inorganic Perovskite Solar Cells, *Nano Lett.*, 2019, **19**, 6213–6220.
44 J. Duan, *et al.*, Inorganic perovskite solar cells: An emerging member of the photovoltaic community, *J. Mater. Chem. A*, 2019, **7**, 21036–21068.
45 Q. Tai, K. C. Tang and F. Yan, Recent progress of inorganic perovskite solar cells, *Energy Environ. Sci.*, 2019, **12**, 2375–2405.
46 P. Wang, *et al.*, Solvent-controlled growth of inorganic perovskite films in dry environment for efficient and stable solar cells, *Nat. Commun.*, 2018, **9**, 2225.
47 T. Moot, *et al.*, CsI-Antisolvent Adduct Formation in All-Inorganic Metal Halide Perovskites, *Adv. Energy Mater.*, 2020, **10**, 1903365.
48 Y. Zheng, *et al.*, High-Performance CsPbIxBr3-x All-Inorganic Perovskite Solar Cells with Efficiency over 18% *via* Spontaneous Interfacial Manipulation, *Adv. Funct. Mater.*, 2020, **30**, 2000457.
49 R. J. Sutton, *et al.*, Bandgap-Tunable Cesium Lead Halide Perovskites with High Thermal Stability for Efficient Solar Cells, *Adv. Energy Mater.*, 2016, **6**, 1502458.
50 G. E. Eperon, *et al.*, Inorganic caesium lead iodide perovskite solar cells, *J. Mater. Chem. A*, 2015, **3**, 19688–19695.
51 G. Mannino, *et al.*, Temperature-Dependent Optical Band Gap in CsPbBr3, MAPbBr3, and FAPbBr3 Single Crystals, *J. Phys. Chem. Lett.*, 2020, **11**, 2490–2496.
52 H. Näsström, *et al.*, Dependence of phase transitions on halide ratio in inorganic CsPb(Br: XI1- x)3perovskite thin films obtained from high-throughput experimentation, *J. Mater. Chem. A*, 2020, **8**, 22626–22631.
53 R. J. Sutton, *et al.*, Cubic or Orthorhombic? Revealing the Crystal Structure of Metastable Black-Phase $CsPbI_3$ by Theory and Experiment, *ACS Energy Lett.*, 2018, **3**, 1787–1794.
54 A. Marronnier, *et al.*, Anharmonicity and Disorder in the Black Phases of Cesium Lead Iodide Used for Stable Inorganic Perovskite Solar Cells, *ACS Nano*, 2018, **12**, 3477–3486.
55 C. A. López, *et al.*, Crystal Structure Features of CsPbBr3 Perovskite Prepared by Mechanochemical Synthesis, *ACS Omega*, 2020, **5**, 5931–5938.
56 Q. Zeng, *et al.*, Polymer-Passivated Inorganic Cesium Lead Mixed-Halide Perovskites for Stable and Efficient Solar Cells with High Open-Circuit Voltage over 1.3 V, *Adv. Mater.*, 2018, **30**, 1705393.
57 W. Xu, *et al.*, Minimizing Voltage Loss in Efficient All-Inorganic CsPbI2Br Perovskite Solar Cells through Energy Level Alignment, *ACS Energy Lett.*, 2019, **4**, 2491–2499.
58 M. Zhai, *et al.*, Construct efficient CsPbI2Br solar cells by minimizing the open-circuit voltage loss through controlling the peripheral substituents of hole-transport materials, *Chem. Eng. J.*, 2021, **425**, 131675.
59 Z. Hawash, L. K. Ono and Y. Qi, Recent Advances in Spiro-MeOTAD Hole Transport Material and Its Applications in Organic–Inorganic Halide Perovskite Solar Cells, *Adv. Mater. Interfaces*, 2018, **5**, 1700623.
60 H. Taherianfard, *et al.*, Perovskite/Hole Transport Layer Interface Improvement by Solvent Engineering of Spiro-OMeTAD Precursor Solution, *ACS Appl. Mater. Interfaces*, 2019, **11**, 44802–44810.
61 W. Yao, *et al.*, Suppression of hysteresis in all-inorganic perovskite solar cells by the incorporation of PCBM, *Appl. Phys. Lett.*, 2021, **118**, 123502.
62 D. H. Kang and N. G. Park, On the Current–Voltage Hysteresis in Perovskite Solar Cells: Dependence on Perovskite Composition and Methods to Remove Hysteresis, *Adv. Mater.*, 2019, **31**, 1805214.

63 J. B. Patel, *et al.*, Influence of Interface Morphology on Hysteresis in Vapor-Deposited Perovskite Solar Cells, *Adv. Electron. Mater.*, 2017, **3**, 1600470.
64 D. Pérez-del-Rey, P. P. Boix, M. Sessolo, A. Hadipour and H. J. Bolink, Interfacial Modification for High-Efficiency Vapor-Phase-Deposited Perovskite Solar Cells Based on a Metal Oxide Buffer Layer, *J. Phys. Chem. Lett.*, 2018, **9**, 1041.
65 L. Cojocaru, *et al.*, Detailed Investigation of Evaporated Perovskite Absorbers with High Crystal Quality on Different Substrates, *ACS Appl. Mater. Interfaces*, 2018, **10**, 26293.
66 J. Li, *et al.*, Highly Efficient Thermally Co-evaporated Perovskite Solar Cells and Mini-modules, *Joule*, 2020, **4**, 1035–1053.
67 T. Abzieher, *et al.*, From Groundwork to Efficient Solar Cells: On the Importance of the Substrate Material in Co-Evaporated Perovskite Solar Cells, *Adv. Funct. Mater.*, 2021, **31**, 2104482.
68 W. Xiang, *et al.*, Europium-Doped CsPbI 2 Br for Stable and Highly Efficient Inorganic Perovskite Solar Cells, *Joule*, 2019, **3**, 205–214.
69 H. Zhao, *et al.*, A Novel Anion Doping for Stable CsPbI2Br Perovskite Solar Cells with an Efficiency of 15.56% and an Open Circuit Voltage of 1.30 V, *Adv. Energy Mater.*, 2019, **9**, 1902279.
70 S. S. Mali, *et al.*, Implementing Dopant-Free Hole-Transporting Layers and Metal-Incorporated CsPbI2Br for Stable All-Inorganic Perovskite Solar Cells, *ACS Energy Lett.*, 2021, **6**, 778–788.
71 J. V. Patil, S. S. Mali and C. K. Hong, A-Site Rubidium Cation-Incorporated CsPbI2Br All-Inorganic Perovskite Solar Cells Exceeding 17% Efficiency, *Sol. RRL*, 2020, **4**, 2000164.
72 J. Pan, X. Zhang, Y. Zheng and W. Xiang, Morphology control of perovskite film for efficient CsPbIBr2 based inorganic perovskite solar cells, *Sol. Energy Mater. Sol. Cells*, 2021, **221**, 110878.
73 Z. Wang, *et al.*, Structured crystallization for efficient all-inorganic perovskite solar cells with high phase stability, *J. Mater. Chem. A*, 2019, **7**, 20390–20397.
74 H. Yu, *et al.*, Strain-Stabilized $CsPbI_3$ Perovskite *via* Organopolysilazane for Efficient Solar Cells with Efficiency over 19, *Adv. Opt. Mater.*, 2022, **10**, 2201672.
75 D. Xue, *et al.*, Regulating strain in perovskite thin films through charge-transport layers, *Nat. Commun.*, 2020, **11**, 1514.
76 Y. Zhang, *et al.*, Moisture assisted CsPbBr 3 film growth for high-efficiency, all-inorganic solar cells prepared by a multiple sequential vacuum deposition method, *Mater. Sci. Semicond. Process.*, 2019, **98**, 39–43.
77 J. M. Kestner, *et al.*, An experimental and modeling analysis of vapor transport deposition of cadmium telluride, *Sol. Energy Mater. Sol. Cells*, 2004, **83**, 55–65.
78 M. J. Bækbo, O. Hansen, I. Chorkendorff and P. C. K. Vesborg, Deposition of methylammonium iodide: *Via* evaporation-combined kinetic and mass spectrometric study, *RSC Adv.*, 2018, **8**, 29899–29908.
79 M. Kroll, *et al.*, Insights into the evaporation behaviour of FAI: material degradation and consequences for perovskite solar cells, *Sustainable Energy Fuels*, 2022, **6**, 3230–3239.
80 I. L. Braly, R. J. Stoddard, A. Rajagopal, A. K. Y. Jen and H. W. Hillhouse, Photoluminescence and Photoconductivity to Assess Maximum Open-Circuit Voltage and Carrier Transport in Hybrid Perovskites and Other Photovoltaic Materials, *J. Phys. Chem. Lett.*, 2018, **9**, 3779–3792.
81 M. Stolterfoht, *et al.*, The impact of energy alignment and interfacial recombination on the internal and external open-circuit voltage of perovskite solar cells, *Energy Environ. Sci.*, 2019, **12**, 2778–2788.
82 L. Krückemeier, U. Rau, M. Stolterfoht and T. Kirchartz, How to Report Record Open-Circuit Voltages in Lead-Halide Perovskite Solar Cells, *Adv. Energy Mater.*, 2020, **10**, 1902573.
83 S. Gharibzadeh, *et al.*, Two birds with one stone: Dual grain-boundary and interface passivation enables >22% efficient inverted methylammonium-free perovskite solar cells, *Energy Environ. Sci.*, 2021, **14**, 5875–5893.
84 M. Grischek, *et al.*, Efficiency Potential and Voltage Loss of Inorganic CsPbI2Br Perovskite Solar Cells, *Sol. RRL*, 2022, **6**, 2200690.
85 S. Pisoni, *et al.*, On the origin of open-circuit voltage losses in flexible n-i-p perovskite solar cells, *Sci. Technol. Adv. Mater.*, 2019, **20**, 786–795.
86 A. Al-Ashouri, *et al.*, Conformal monolayer contacts with lossless interfaces for perovskite single junction and monolithic tandem solar cells, *Energy Environ. Sci.*, 2019, **12**, 3356–3369.
87 M. Cesaria, A. P. Caricato and M. Martino, Realistic absorption coefficient of ultrathin films, *J. Opt.*, 2012, **14**, 105701.